

Disconnecting the Dots: Re-Examining the Nature of Stellar “Strings” in the Milky Way

CATHERINE ZUCKER ¹, J. E. G. PEEK ^{1,2} AND SARAH LOEBMAN ³

¹*Space Telescope Science Institute, 3700 San Martin Drive, Baltimore, MD 21218, USA**

²*Department of Physics & Astronomy, Johns Hopkins University, Baltimore, MD 21218, USA*

³*Department of Physics, University of California, Merced, 5200 Lake Road, Merced, CA 95343, USA*

ABSTRACT

Recent analyses of *Gaia* data have resulted in the identification of new stellar structures, including a new class of extended stellar filaments called stellar “strings”, first proposed by Kounkel & Covey (2019). We explore the spatial, kinematic, and chemical composition of strings to demonstrate that these newfound structures are largely inconsistent with being physical objects whose members share a common origin. Examining the 3D spatial distribution of string members, we find that the spatial dispersion around the claimed string spine does not improve in the latest *Gaia* DR3 data release — despite tangible gains in the signal-to-noise of the parallax measurements — counter to expectations of a bona fide structure. Using the radial velocity dispersion of the strings (averaging $\sigma_{V_r} = 16 \text{ km s}^{-1}$) to estimate their virial masses, we find that all strings are gravitationally unbound. Given the finding that the strings are dispersing, the reported stellar ages of the strings are typically $120\times$ larger than their measured dispersal times. Finally, we validate prior work that stellar strings are more chemically homogeneous than their local field stars, but show it is possible to obtain the same signatures of chemical homogeneity by drawing random samples of stars from spatially, temporally, and kinematically unrelated open clusters. Our results show that while some strings may be composed of real substructures, there is no consistent evidence for larger string-like connections over the sample. These results underline the need for caution in over-interpreting the significance of these strings and their role in understanding the star formation history of the Milky Way.

1. INTRODUCTION

It is commonly accepted that most stars in the Milky Way were born in close proximity to other stars, constituting a stellar structure that formed at the same time within the same parental molecular gas structure (e.g. Lada & Lada 2003). These stellar siblings should be similar to one another in terms of their location, age, kinematics, and chemistry. As these stellar structures dissolve into the Galactic field, they offer an opportunity to study the star formation history of the Milky Way and the chemodynamical evolution of its disk. As the largest and most accurate astrometric catalog of stars ever produced, *Gaia* (Gaia Collaboration et al. 2016) offers an unprecedented opportunity to study these stellar structures from their formation to their dissolution. By constraining the distances and proper motions to over a billion stars, as well as the radial velocities of millions of stars, *Gaia* has not only shed new light on the spatial and dynamical properties of existing stellar structures, but has also enabled the discovery of new ones. These discoveries include hundreds of previously unknown open clusters (e.g. Castro-Ginard et al. 2020), as well as new classes of stellar structures with much more extended spatial distributions (see e.g. discussion in §3.5 of Cantat-Gaudin 2022), including stellar “streams” in the Galactic disk (Meingast et al. 2019), extended stellar coronae (Meingast et al. 2021; Ratzenböck et al. 2020; Meingast & Alves 2019), stellar “pearls” (Coronado et al. 2022), stellar “relic filaments” (Jerabkova et al. 2019; Beccari et al. 2020), stellar “snakes” (Wang et al. 2022), and stellar “strings” (Kounkel & Covey 2019) (see also Kounkel et al. 2020).

In Table 1, we compare and contrast the properties of these proposed extended stellar structures, including their velocity dispersions, claimed co-evality, gravitational boundedness, lengths, and widths. All extended structures have

Corresponding author: Catherine Zucker
czucker@stsci.edu

* Hubble Fellow

similar lengths (spanning $\approx 100 - 400$ pc) and widths (\approx few tens of parsecs) with typical aspect ratios between 3:1 and 10:1. None of the studies in Table 1 explicitly require the structures to be gravitationally bound, though Kounkel & Covey (2019) argue that strings are “weakly bound” while Meingast et al. (2019) and Meingast et al. (2021) argue that the recently discovered streams in the disk and extended coronae around open clusters are gravitationally unbound. All structures are argued to be co-eval with the exception of stellar “pearls”, which are distinct clusters following similar orbits in the Galaxy that manifest as overdensities in action-angle space (Coronado et al. 2022). Stellar strings are similar to stellar “snakes” and stellar “relic filaments” in that all three structures are identified in part via clustering algorithms in 5D space (e.g. HDBSCAN, DBSCAN, Friends-of-Friends) and have radial velocity dispersions spanning $\approx 5 \text{ km s}^{-1}$ (relic filaments) to $\approx 15 \text{ km s}^{-1}$ (strings). The filamentary structure seen in strings, snakes, and relic filaments is argued to be primordial, likely forming in elongated giant molecular filaments (Goodman et al. 2014; Zucker et al. 2015, 2018; Ragan et al. 2014; Wang et al. 2015; Zucker et al. 2019). In contrast, stellar streams in both the disk (Meingast et al. 2019) and the halo (Gialluca et al. 2021; Kuzma et al. 2015), as well as recently discovered extended stellar coronae (Meingast et al. 2021), have much smaller velocity dispersions ($\approx 1 \text{ km s}^{-1}$) with the filamentary structure forming as a result of dynamical tidal forces dissolving a central cluster.

There are four attributes that members of a newly discovered stellar structure (like those in Table 1) should share in order to plausibly be considered co-eval, or born at the same time within the same parental molecular gas structure. First, stars in a structure should have largely similar ages. Second, members of a stellar structure should be close enough to one another in 3D space such that they could have been born in the same location. Third, members of a stellar structure should share similar motions, as evidenced by small dispersion in their *Gaia* tangential and radial velocities. Finally, members of a stellar structure should have similar metallicities, as evidenced by small dispersion in elemental abundances (e.g. as measured by spectroscopic surveys like GALAH and APOGEE; Buder et al. 2021; Jönsson et al. 2020).

With these attributes in mind, we take a closer look at the spatial, kinematic, and abundance variations of the most extreme population in Table 1 – the stellar strings – first proposed by Kounkel & Covey (2019) (hereafter KC19). KC19 present a sample of 328 claimed co-eval stellar strings. While KC19 do not quantitatively define a string, they argue that strings should appear to be filamentary, roughly parallel to the Galactic plane, coherent both spatially and kinematically, and that their stellar members can generally be characterized with a single isochrone. The median projected length and width of a string is 190 pc and 30 pc, respectively.

KC19 identify the strings in a multi-step process. First, they apply the HDBSCAN algorithm (McInnes et al. 2017) in 5D space (l , b , parallax π , and proper motions) to a sample of stars out to 1 kpc from the Sun detected in *Gaia* DR2. Specifically, they perform several iterations of the HDBSCAN algorithm over different parallax ranges, primarily with the “leaf” clustering method, to obtain a set of stellar groups with similar 5D properties. Then the authors manually merge and split the groups detected in the various iterations by hand. Next, KC19 assign an age to each group using a combination of isochrone fitting and a convolutional neural network. Finally, once a sample of stellar groups is identified via HDBSCAN, KC19 manually assemble the strings by either i.) connecting the individual groups with similar ages using the tool TOPCAT (Taylor 2005) or ii) deciding that a single group possesses enough filamentary morphology to be classified as a string. Finally, KC19 visually check that the strings are “fully continuous [and] coherent in all kinematic [i.e. tangential velocities] and spatial [i.e. l , b , π] dimensions.” After the groups are connected, KC19 compute a “spine” for the string in 5D space by averaging the star-by-star (l , b , π , and kinematics) results in different plane-of-the-sky longitude bins along the projected string, before smoothing with a Savitzky-Golay filter to avoid strong fluctuations in the averages.

In this work, we independently test the kinematic, spatial, and chemical coherence of the stellar strings using data not fully considered by and/or available at the time of KC19. In §2 we present the publicly available spatial and kinematic data for stellar strings from *Gaia* DR2 and DR3 utilized in this work, along with ancillary spectroscopic data used to examine the elemental abundance variations within a subset of the strings. In §3 we use these data to derive estimates of the stars’ 3D spatial dispersion around their respective string “spines”, their radial velocity dispersions, their predicted virial masses, their predicted dynamical lifetimes, and their elemental abundance variations. We then use these constraints to show that nearly all of these stellar strings are inconsistent with being co-eval, physical entities, and are rather artificial structures affected by limitations in the manual assembly process used in their selection. In §4 we discuss the implications of the strings’ nonphysical nature within the wider context of the *Gaia* literature on extended stellar structures. Finally, we conclude in §5.

Table 1. Proposed Extended Stellar Structures in the Galactic Disk

Name	ID	Claimed Co-Eval?	σ_{V_r}	Length	Width	Bound?	Formation	Publication
(1)	(2)	(3)	(4)	(5)	(6)	(7)	(8)	(9)
String	HDBSCAN (5D)	Yes	15	200	30	Weakly Bound	Primordial Filaments	Kounkel & Covey (2019) Kounkel et al. (2020)
Snake	FoF (5D)	Yes	10	200	90	Not claimed	Primordial Filaments	Tian (2020) Wang et al. (2022)
Relic Filament	DBSCAN (5D)	Yes	5	90 - 260	10 - 50	Not claimed	Primordial Filaments	Jerabkova et al. (2019) Beccari et al. (2020)
Extended Corona	Convergent Point (Deproj. 5D)	Yes	1	100 - 400	50 - 75	Unbound	Tidally Disrupted Clusters	Meingast et al. (2021)*
Stream	Wavelet Decomposition (6D)	Yes	1	400	50	Unbound	Tidally Disrupted Cluster	Meingast et al. (2019) Ratzenböck et al. (2020)
Pearl	Orbit-Phase Space FoF (6D)	No	—	—	—	Unbound	Primordial Filaments	Coronado et al. (2022)

NOTE—Comparison of the identification, properties, and physical interpretation of extended stellar structures recently discovered in the *Gaia* era. (1) Name of the extended stellar structure (2) *Primary* identification method of the structure, specifying whether initial identification was made in 5D (not including radial velocities) or 6D (including radial velocities) space. See the references below for full details on the multi-step structure identification. (3) Whether the structures are claimed to be co-eval in their original publications. (4) Typical radial velocity dispersion of the structure. (5) Average length or the range of lengths over the sample. (6) Average width or range of widths over the sample. (7) Whether the structures are suggested to be bound or unbound in their original publications. (8) The proposed formation mechanism for the structures, specifically whether their filamentary morphology is argued to be primordial (in filamentary giant molecular clouds) or whether it is the result of tidal stretching dissolving a central cluster. (9) Original publications describing identification and properties of the proposed extended stellar structures. No length, width, or radial velocity dispersion are provided for the pearls, as they are not argued to be monolithic structures, but rather sets of distinct clusters that follow similar orbits.

* See also Moranta et al. (2022) for extended coronae identified in 5D space via HDBSCAN

2. DATA

KC19 identify 1312 stellar groups and 328 stellar strings. A group is a single set of stars identified in HDBSCAN with similar 5D properties (l , b , parallax π , and proper motions), while a string is either a collection of connected HDBSCAN groups or a single HDBSCAN group deemed to be filamentary in KC19. We only consider the stellar strings in this work. We obtain the *Gaia* DR2 data (Gaia Collaboration et al. 2018) (sky coordinates, parallaxes, and parallax errors) on the string stars directly from KC19 (see their Table 1), and we crossmatch their Table 1 with *Gaia* DR3 (Gaia Collaboration et al. 2021) to obtain updated constraints on the parallax and parallax errors of the string stars. The XYZ positions (the Heliocentric Galactic Cartesian Coordinates) of string spines (defined using *Gaia* DR2 data) are obtained from Table 3 in KC19 and will be used to calculate the 3D dispersion of string members around their respective spines in §3.1. To analyze the kinematic coherence of the strings in §3.2, we adopt the updated radial velocity measurements from *Gaia* DR3, which provides radial velocity data for $\approx 5\times$ more stars than available in *Gaia* DR2 in KC19. To explore the metallicity distribution within the strings, we use the catalog from Manea et al. (2022, hereafter MHM22). MHM22 leverages GALAH DR3 (Buder et al. 2021) elemental abundance measurements (e.g. $[\text{Fe}/\text{H}]$) and their reported uncertainties to analyze the chemical homogeneity of stars in nearby stellar structures, including ten strings (see their Supplementary Data). To compare the chemical homogeneity of the strings to a benchmark sample of open clusters, we adopt the catalog from Spina et al. (2021) (see their Table 1), which compiles a similar set of elemental abundance measurements from GALAH (Buder et al. 2021) and APOGEE (Jönsson et al. 2020) for a sample of stars in hundreds of open clusters across the Galactic disk.

3. THE SPATIAL, DYNAMICAL, AND CHEMICAL COMPOSITION OF STELLAR STRINGS

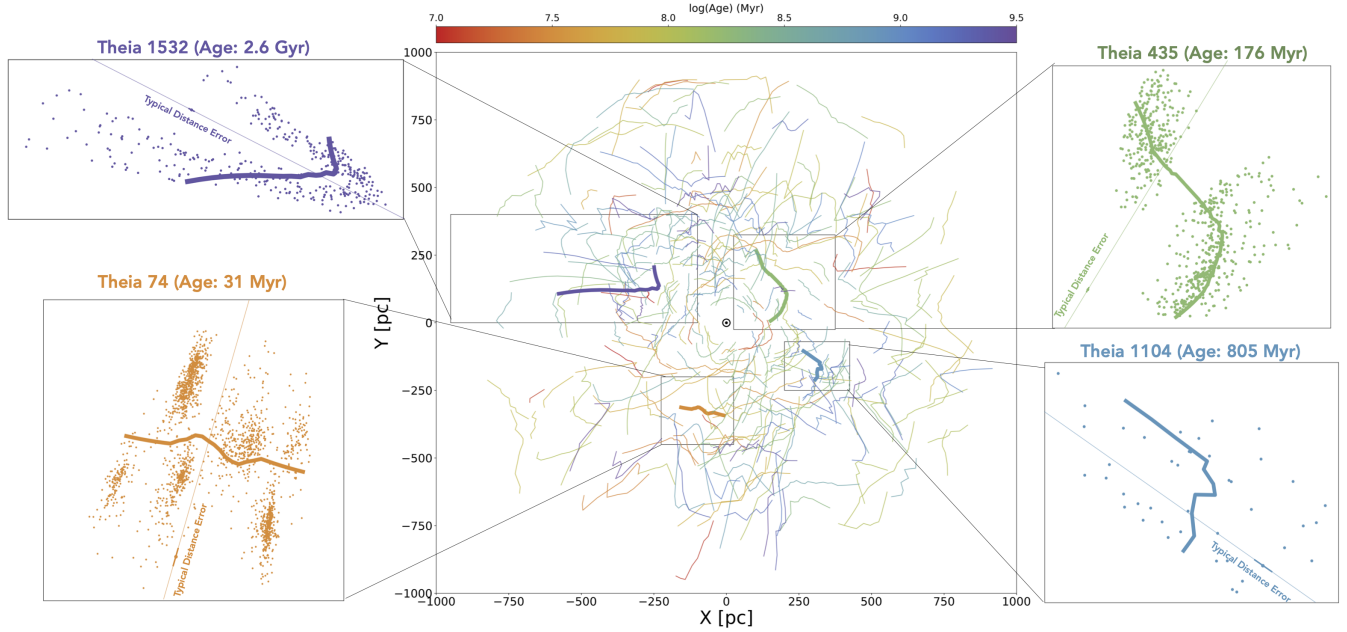


Figure 1. *Center:* A topdown view of stellar strings, colored by age, based on KC19 (see their Figure 13). In the zoom-in boxes, we show the actual distribution of stellar members around the string “spine” in *Gaia* DR2 for a sub-sample of four strings spanning a range of ages. The typical distance error to stars is very small with N average parallax signal-to-noise > 44 in *Gaia* DR2. Since the strings “spines” are derived using *Gaia* DR2 data, these DR2 stellar distributions are the actual data used to derive the string properties in KC19. We find that these four strings are representative of the morphology seen across the full sample: the dispersion along the line of sight is significantly larger than the typical error on the parallax measurements (e.g. Theia 1532, Theia 1104), and many strings are composed of isolated groups with no evidence of connection between them (e.g. Theia 74, Theia 435). See Figure Set A1 in the Appendix or the [online interactive figure gallery](#) for similar panels for the remaining strings in the KC19 sample, as well as additional comparisons to the *Gaia* DR3 stellar distributions.

In this section, we re-examine the spatial (§3.1), dynamical (§3.2), and chemical (§3.3) distribution of the strings in KC19 and present a summary of their derived properties in Table 2.¹

3.1. 3D Spatial Properties of Stellar Strings

In Figure 1 we show a topdown XY *Gaia* DR2 view of the stellar strings as reproduced from KC19 (see their Figure 13). We highlight a selection of strings (over a range of ages) to convey the relationship between each string and its underlying stellar membership. Similar plots for the rest of the string sample are shown in Figure Set A1 in the Appendix. The distances to the string stars are very well constrained: the median signal to noise of the parallax measurements per string surpasses 44:1 in DR2 and 61:1 in DR3. For a majority of the strings, the dispersion around the spine is much larger than the average distance uncertainty. Many strings are composed of discrete stellar groups that lack clear connections in 3D physical space, despite that interpretation in KC19.

Leveraging the improved astrometric precision of *Gaia* DR3, we compare the 3D spatial dispersion of stars around the string spine in *Gaia* DR2 versus *Gaia* DR3 to determine whether the dispersion around the spine decreases as parallax errors improve, as expected of real structures. For each star, we compute its 3D offset from the string’s spine in *Gaia* DR2 and DR3, and then average the results per string. The results are presented in Figure 2, which shows the average percentage that the stars move closer to or further from the spine as a function of the increase in the signal to noise of the parallax measurements. Despite the signal to noise of the parallaxes improving by 20%–120% in *Gaia* DR3, there is *no improvement* in the stars’ offsets from the spines. The lack of improvement in the stars’ 3D spatial dispersion is inconsistent with the claim that strings are co-eval, physical entities whose members share a common origin. However, we do observe (c.f. Figure Set A1 in the Appendix and the [online interactive figure gallery](#)) that in

¹ On [Zenodo](#), we provide a Jupyter Notebook that reproduces all the results in this section, including the values in Table 2, and the data behind Figures 1, 2, 3, 4 and 5 (doi:10.5281/zenodo.6984474).

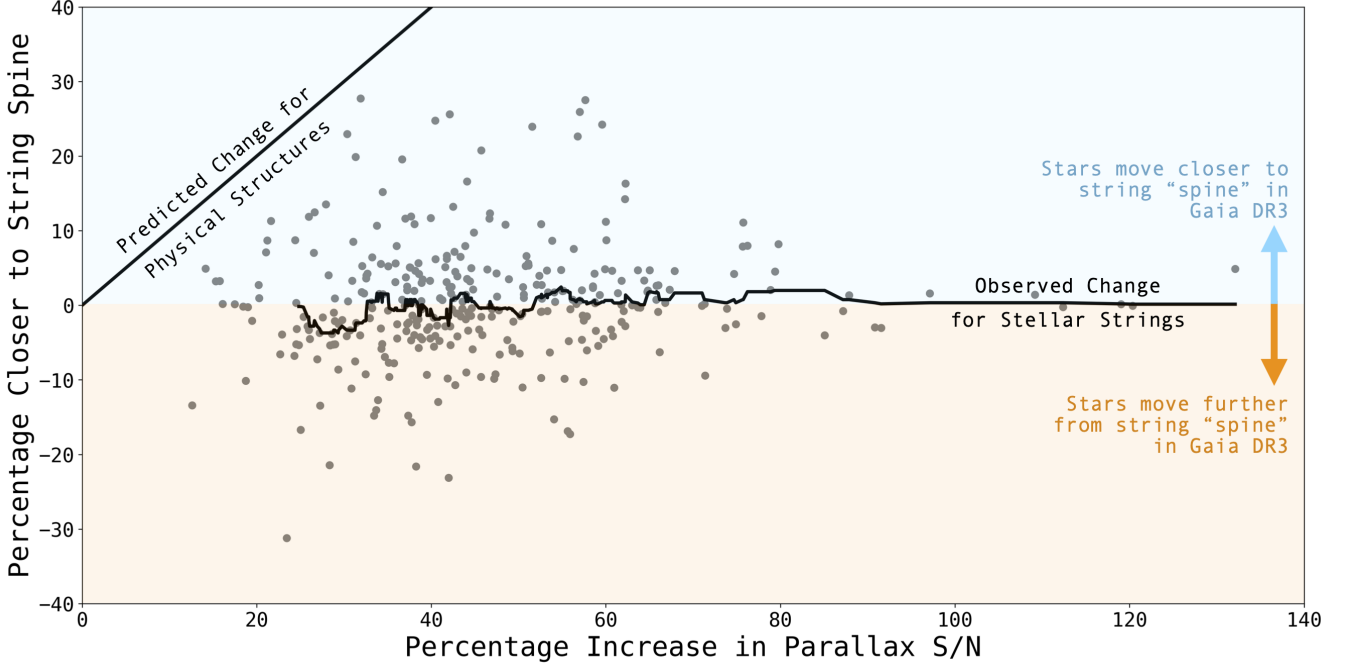


Figure 2. Change in the 3D spatial dispersion of stars around their string’s spine from *Gaia* DR2 to *Gaia* DR3. Each grey dot represents one of the 328 individual strings. The dots show the average percentage change in the 3D spatial offset from the spine as a function of the average increase in the signal-to-noise of the parallax measurements for the stars. Positive percentage (blue region) indicates the stars move closer to their spine with improved parallax measurements, while negative percentage (orange region) indicates they move farther away. The black line shows the rolling median and indicates that despite a significant improvement in the signal-to-noise of the parallax measurements, the dispersion around the spine does not improve on average as expected of genuine spatial structures. The diagonal line in the top left shows the predicted trend for genuine space structures.

some cases the 3D spatial dispersion within *individual* stellar groups inside a string does improve. This suggests these strings may be partly composed of real stellar subgroups; however, we see no evidence for the larger string connections.

3.2. The Dynamical Properties of Stellar Strings

While the lack of improvement in the 3D spatial dispersion of stars around the string spines raises concerns about their fidelity, one way to validate the authenticity of the strings is to show that their stellar members still share similar motions. KC19 analyze the dispersion in the tangential velocities of string members and find them to be $< 2.5 \text{ km s}^{-1}$. We expect a small dispersion in the tangential velocities, since the stellar groups that were manually assembled into strings must share similar 5D properties (l , b , parallax π , and proper motions) to be detected with HDBSCAN. As such, the fairest way to evaluate the authenticity of the strings is to characterize their velocity dispersion in the sixth dimension — the radial velocity dimension — not considered in the original 5D clustering algorithm. KC19 find that the dispersion in the radial velocities, σ_{V_r} , span $5 - 40 \text{ km s}^{-1}$ with an average radial velocity dispersion of 16 km s^{-1} , a factor of $5 - 10\times$ larger than for the tangential velocities (see Figure 12 from KC19). The typical *Gaia*-based radial velocity dispersion for loosely bound open clusters is $\approx 1 \text{ km s}^{-1}$ (Soubiran et al. 2018), making these strings at least dynamically very atypical for known co-eval structures.

Leveraging the expanded catalog of radial velocities in *Gaia* DR3 — providing $5\times$ more measurements than available at the time of KC19 — we compute updated, error-weighted radial velocity dispersions for the strings. Before calculating the error-weighted radial velocity dispersion, we mask out stars classified as astrometric, spectroscopic, or eclipsing binaries in *Gaia* DR3 by requiring the `non_single_star` flag to be 0. We adopt the same methodology used in Soubiran et al. (2018) to calculate the error-weighted radial velocity dispersion for open clusters:

$$\sigma_{V_r}^2 = \frac{\sum_i w_i}{(\sum_i w_i)^2 - \sum_i w_i^2} \sum_i w_i (RV_i - RV_{\text{str}})^2 \quad (1)$$

where w_i is the weight for the i th star ($w_i = \frac{1}{RV_{err,i}^2}$), $RV_{err,i}$ is the star’s radial velocity error, RV_i is the star’s radial velocity measurement, and RV_{str} is the error-weighted mean velocity of all stars in the string. Despite significantly enlarging the radial velocity sample, removing known binaries, and implementing error-weighting, the average string radial velocity dispersion stays the same at 16 km s^{-1} . Figure 3 shows the distribution of error-weighted radial velocity dispersion for the strings as a function of their reported ages from KC19, alongside comparable measurements for extended stellar coronae and stellar streams in the disk (see Table 1).

Using the updated radial velocity dispersions, we estimate the predicted virial mass of each string as:

$$M_{vir} = \frac{\sigma_{V_r}^2 \times \eta \times r_{hm}}{G} \quad (2)$$

where r_{hm} is the adopted half-mass radius of the string. The parameter η is a dimensionless constant that depends on the shape of the density profile, for which we very conservatively adopt $\eta = 1$.² We find that the average predicted virial mass of the strings is $\approx 2 \times 10^6 M_\odot$. We approximate the observed mass of each string by counting the number of members and assuming an average stellar mass of $0.61 M_\odot$ based on the Initial Mass Function from Maschberger et al. (2010) (see also e.g. Kuhn et al. 2019). We find a typical observed mass of $M_{observed} = 134 M_\odot$, meaning that strings on average require $> 10^4 \times$ larger masses than their observed masses to be in virial equilibrium. Even assuming a very poor completeness fraction, all strings are gravitationally unbound, counter to the claim in KC19 that strings are “weakly bound.”

While the unbound state of the strings does not in itself imply that strings are unphysical, it does provide constraints on their predicted lifetimes. If a string is gravitationally unbound, it should disperse on roughly a crossing time, t_{cross} :

$$t_{dispersal} \approx t_{cross} \approx \frac{r_{hm}}{\sigma_{V_r}} \quad (3)$$

We find a median predicted dispersal time for the strings of only 2 Myr. Since KC19 determine ages of between 4 Myr and 9 Gyr for the strings, the strings’ reported ages are on average $126 \times$ larger than their dispersal times. In Figure 4 we plot $\frac{M_{virial}}{M_{observed}}$ as a function of $\frac{\text{Reported Age}}{\text{Dispersal Time}}$. Since the strings should have already dispersed in a fraction of their reported lifetimes, their kinematics are likewise inconsistent with the claim that strings are co-eval, physical entities whose members share a common origin.

3.3. The Chemical Homogeneity of Stellar Strings

We perform a final test to determine the physicality of the stellar string members by examining the uniformity in their chemical composition with respect to open cluster members. If a set of stars is born within the same parental molecular gas structure, they should be chemically homogeneous (e.g. Feng & Krumholz 2014). To examine the chemical homogeneity of the strings, we build off the study of Manea et al. (2022, MHM22), who leverage GALAH data (Buder et al. 2021) to characterize the intrinsic chemical dispersion ($\sigma_{[X/H]}$) of a sample of ten strings. MHM22 fit the following likelihood function assuming that the chemical profile of each string is Gaussian with some mean abundance $\mu_{[X/H]}$ and intrinsic dispersion $\sigma_{[X/H]}$:

$$\mathcal{L} = \prod_i^N \exp \left[\frac{-(x_i - \mu_{[X/H]})^2}{2(\sigma_{[X/H]}^2 + \delta_i^2)} \right] \times \frac{1}{\sqrt{2\pi(\sigma_{[X/H]}^2 + \delta_i^2)}} \quad (4)$$

where x_i and σ_i are the GALAH mean abundance and its reported uncertainty for the i th star in the string in a given element X. MHM22 characterize the intrinsic chemical dispersion across a range of elements with a sample size between 7 and 19 stars per string. In the left panel of Figure 5, we reproduce the original results of MHM22 (see their Figure 4), showing the intrinsic dispersion $\sigma_{[X/H]}$ for each of the ten strings. MHM22 find that all but one of the strings is more homogeneous than their local field stars, with half of the sample as homogeneous as the well-studied open cluster M67 in several elements (Gao et al. 2018).

To test whether it is possible for a string to appear chemically homogeneous in several elements *without* being co-eval, we draw random sub-samples of stars from the Spina et al. (2021) catalog, who curate a sample of open cluster

² The η parameter is typically assumed to be ≈ 10 for a Plummer model (Plummer 1911) characterized by steep density profiles. Since recent studies have shown that η can be smaller (consistent with much broader density profiles), particularly for younger systems due to e.g. mass segregation (Portegies Zwart et al. 2010), we adopt a much lower value of $\eta = 1$ as larger values of η will only raise the threshold necessary for the strings to be in virial equilibrium.

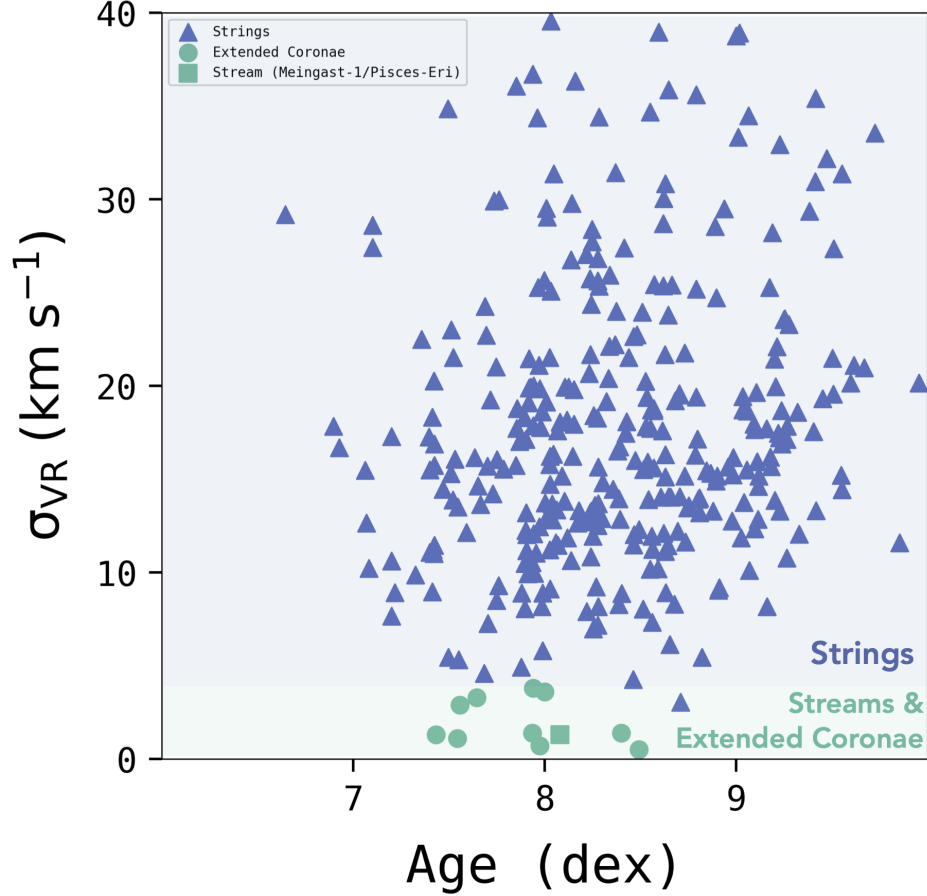


Figure 3. Error-weighted radial velocity dispersions of the strings as a function of their reported ages in KC19. Alongside the strings, we show comparable measurements for the extended stellar coronae (Meingast et al. 2021) around nearby open clusters (including e.g. the Pleiades and α Per) and the stellar streams (Meingast-1/Pisces-Eridanus; see Meingast et al. 2019; Hawkins et al. 2020) summarized in Table 1.

members detected in GALAH. Specifically, following MHM22, we draw between 7 and 19 per sub-sample and restrict to open clusters which span the same broad age range for the strings considered in MHM22 ($7.52 < \log(\text{Age}) < 9.23$), have a detection in GALAH, and high membership probability $p > 0.75$. These sub-samples consist of stars that do *belong to well-studied open clusters*, but each sub-sample is drawn from many clusters that are *unrelated*. We then fit the same likelihood function as MHM22, repeating this procedure over many trials. Since we argue strings are likely agglomerations of unrelated open clusters and other dynamically cold field stars, this experiment provides a more direct comparison point to interpret apparent homogeneity found in MHM22.

As seen in Figure 5, we can match the chemical homogeneity of the strings with the random draws, which we attribute to two causes. First, the uncertainties on the GALAH abundance variations for an individual star i (i.e. σ_i in Equation 4) are similar to the intrinsic abundance variation of a cluster like M67 ($\sigma_i \approx \sigma_{[X/H]} \approx 0.1$ dex). Since Equation 4 is designed to capture the intrinsic uncertainty by modeling the observational error, any overestimation of the error in GALAH can lead to unrealistically small estimates for the intrinsic scatter when the errors are large. And second, these random sub-samples can appear more homogeneous than field stars simply by virtue of the stars being members of open clusters, even if these clusters are physically unrelated.³

Our results are consistent with the scenario that, while these strings may sometimes contain real clusters, their abundance patterns are not discriminatory enough to favor a scenario where members of the string have the same

³ The local field star sample from Manea et al. (2022) (showing poorer chemical homogeneity than the strings) also likely includes some thick disk stars, which will have a wider metallicity dispersion than the thin disk string stars selected by KC19.

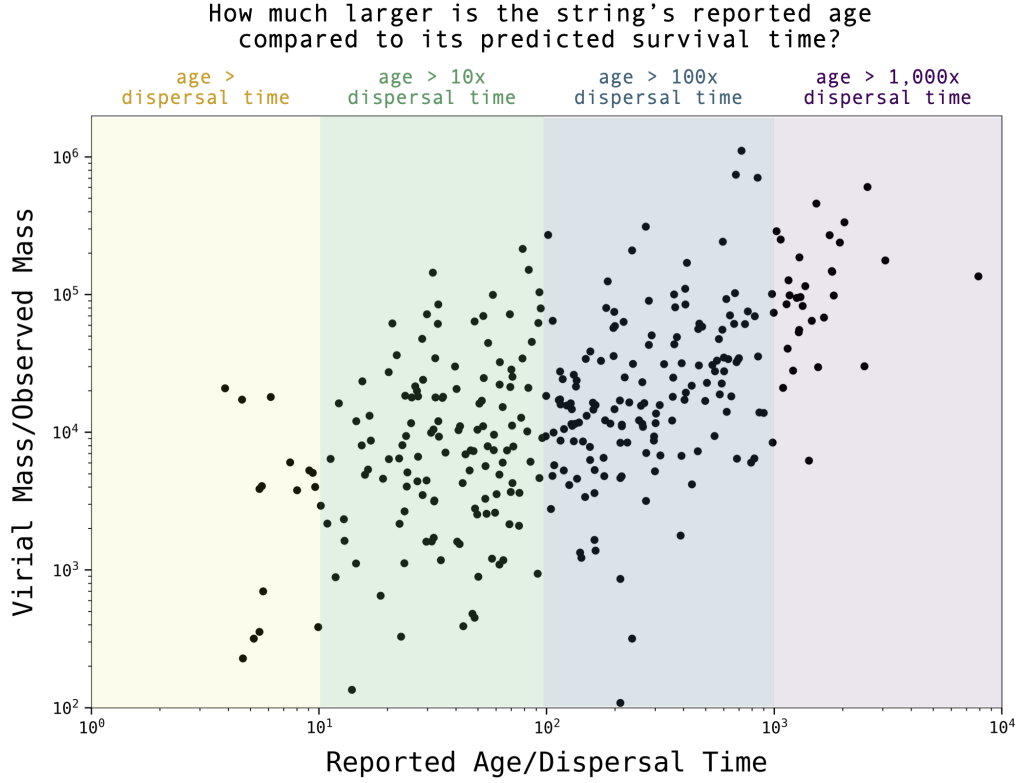


Figure 4. The virial state of strings versus the discrepancy between the strings’ reported and predicted lifetimes. The vertical axis shows the ratio of the predicted virial masses of the strings (based on their observed radial velocity dispersions) over their observed masses. Every string in the sample is gravitationally unbound, requiring on average of 2×10^4 times larger mass than observed to be in virial equilibrium. Given their unbound state, the dispersal time of the strings should be roughly the crossing time. As shown on the horizontal axis, we find that the reported ages of the strings are orders of magnitude larger than the dispersal time, meaning that strings should have dispersed in a small fraction of their reported lifetimes and are thus inconsistent with being physical structures.

origin, versus a range of origins in potentially real, yet physically unrelated, spatial sub-structures. The chemical homogeneity of the strings found in MHM22 does not show them to be co-eval.

4. DISCUSSION

Through a spatial, kinematic, and chemical re-analysis of their stellar membership, we have shown that strings are inconsistent with being co-eval stellar structures with a common physical origin. KC19 select all 328 strings through a manual assembly process, stitching together stellar groups by hand and visually confirming kinematic and spatial coherence by eye. Our work underlies the need for a more systematic, *reproducible* selection process when declaring the existence of a new type of stellar structure: not only should these structures remain spatially coherent and continuous when viewed in true 3D physical space, but their radial velocity dispersions should also be significantly smaller than measured for the Galactic field. In the solar neighborhood, the age-velocity dispersion relation (describing how the velocity dispersion of stars appears to increase with age due to dynamical heating) shows typical vertical velocity dispersions of $\approx 5 \text{ km s}^{-1}$ for stars $< 1 \text{ Gyr}$, about $3\times$ smaller than the typical string radial velocity dispersion of 16 km s^{-1} (see Bird et al. 2021; Casagrande et al. 2011). The age-velocity dispersion relation has also been explored in 3D using open clusters. Specifically, for open clusters in the same age range as the typical string (150 - 250 Myr), Tarricq et al. (2021) find a 3D velocity dispersion of 13 km s^{-1} , meaning that the velocity dispersion *over* a sample of many open clusters is less than the typical radial velocity dispersion *within* an individual string in KC19 (see Figure 11, Table 3 in Tarricq et al. 2021).

While we argue against the physicality of strings in KC19, several other studies in the *Gaia* era present compelling evidence for filamentary stellar distributions identified through more reproducible selection algorithms, some of which are summarized in Table 1. Meingast et al. (2019) identify an extended 400+ pc long, $2000 M_{\odot}$ stream in the

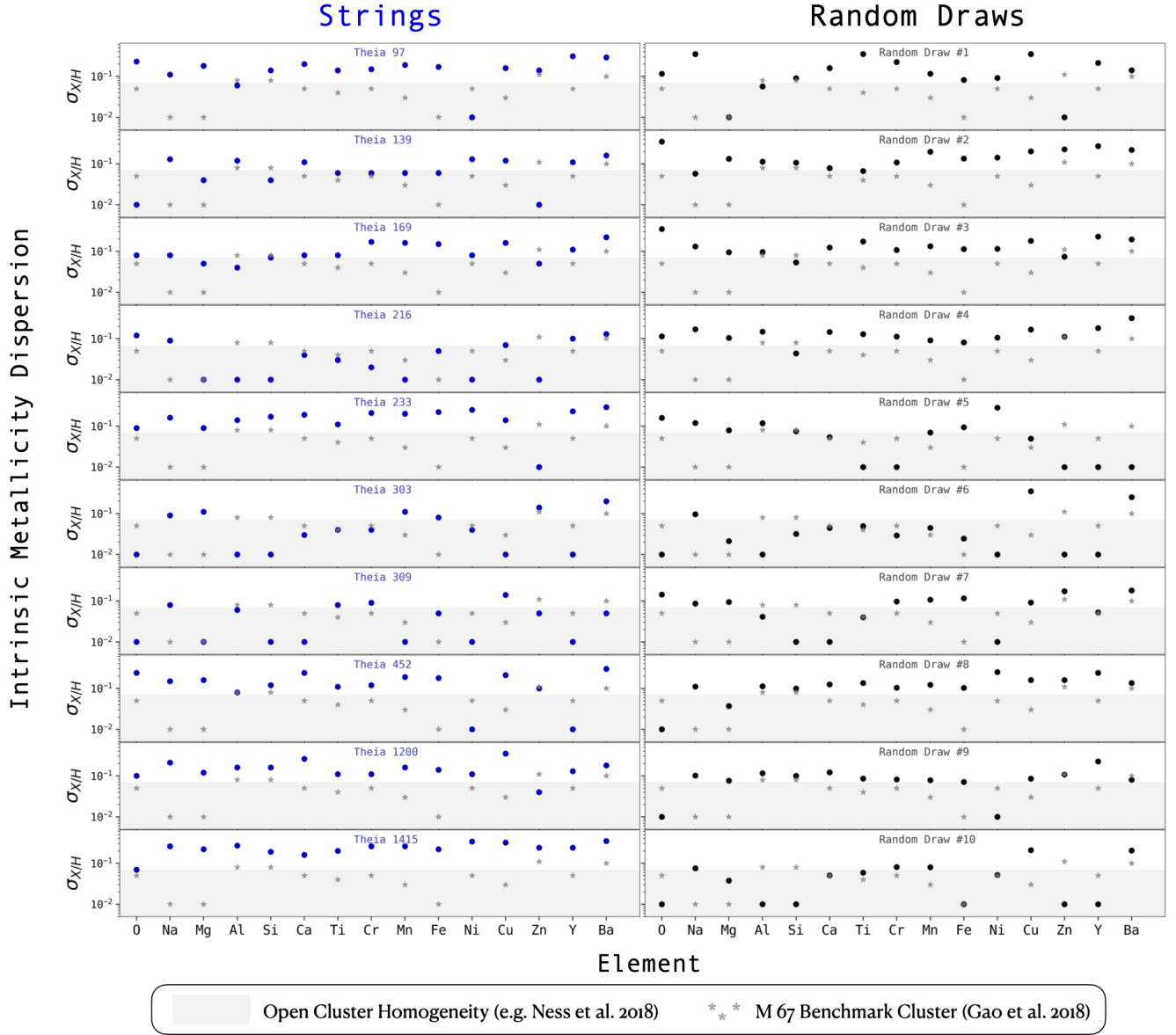


Figure 5. Intrinsic abundance variations across fifteen different elements for the collection of ten strings from MHM22 (blue points, left) and ten random sub-samples of stars drawn from unrelated open clusters in the Milky Way (black points, right). The grey asterisks in each panel show the intrinsic abundance variations for the benchmark cluster M67 (Gao et al. 2018; Manea et al. 2022), while the gray shaded region marks the zone of reported open cluster dispersions (e.g. Ness et al. 2018). By drawing random samples of stars from unrelated clusters, we are able to reproduce the typical chemical homogeneity of a majority of the strings, indicating that the strings’ abundance variations are not discriminatory enough to favor a common physical origin. An interactive version of this figure showing hundreds of random draws, rather than just ten, is available online [here](#).

disk called Meingast-1 (also known as Pisces Eridanus; e.g. Hawkins et al. 2020) through a wavelet decomposition of the 3D velocity space distribution of nearby stars. Not only do Meingast et al. (2019) find that the stream is spatially continuous in 3D space but they also find a 3D velocity dispersion of 1.3 km s^{-1} . Similarly, Meingast et al. (2021) present a new method for identifying highly extended coronae around ten nearby open clusters. The Meingast et al. (2021) technique accounts for projection effects in proper motion space in an automated way (inspired by the “convergent point technique”; c.f. van Leeuwen 2009) before deconvolving the spatial distribution with a Gaussian mixture model to mitigate *Gaia* measurement errors. The coronae are likewise validated via their 3D space motions, showing typical 3D velocity dispersions of 1.4 km s^{-1} .

Both the extended coronae and the Meingast-1 stream have velocity dispersions on par with open clusters. Using a sample of a few hundred nearby open clusters, [Soubiran et al. \(2018\)](#) find typical intra-cluster radial velocity dispersion of $1.0 - 1.5 \text{ km s}^{-1}$. Only four strings in KC19 have radial velocity dispersions $< 5 \text{ km s}^{-1}$ (Theia 127, 161, 605, and 998), while $\approx 90\%$ of the open clusters do ([Soubiran et al. 2018](#)), as well as 100% of the newly identified extended structures in [Meingast et al. \(2019\)](#) and [Meingast et al. \(2021\)](#). The unphysical nature of the strings is not due to their claimed unique filamentary morphologies, but rather their lack of true 3D kinematic and spatial coherence stemming from limitations in the manual assembly process. Since we argue that some strings can be composed of open clusters and other dynamically cold field stars, dedicated follow-up studies (e.g. [Andrews et al. 2022](#)) would be needed to characterize the extent to which individual strings may contain physically relevant sub-structure.

5. CONCLUSIONS

We investigate the spatial, dynamical, and chemical composition of stellar strings, a proposed collection of highly extended filamentary stellar structures identified in KC19 by manually linking stellar groups with similar 5D properties (l , b , parallax π , and proper motions). Our conclusions are as follows:

1. Using updated constraints on the distances to stellar string members from *Gaia* DR3, we find that the 3D spatial dispersion of stars around the string spine does not improve over *Gaia* DR2: the average percentage that stars move closer to their respective string spines is consistent with zero, despite the signal to noise on the parallax measurements per string increasing by 20% - 120%. Real structures should tighten with higher fidelity distance measurements.
2. The average dispersion in the radial velocity of the strings is 16 km s^{-1} , about fifteen times larger than the typical radial velocity dispersion both of open clusters in *Gaia* ([Soubiran et al. 2018](#)) and in other catalogs of extended stellar structures (e.g. stellar “streams” in the disk from [Meingast et al. 2019, 2021](#)).
3. Given the radial velocity dispersions, the virial masses of the strings are on average $> 10^4\times$ larger than their observed masses. Even assuming very low completeness fractions, all strings are gravitationally unbound.
4. Given their unbound state, the strings should disperse on roughly a crossing time, which we estimate to be typically 2 Myr, while the ages of the strings from KC19 range from 4 Myr to 9 Gyr. Thus the strings should not exist based on their predicted dynamical lifetimes, and should have dispersed in $< 1\%$ of their reported ages, on average.
5. Using complementary constraints on stellar chemical abundances from GALAH DR3 ([Buder et al. 2021](#)), we compare the intrinsic abundance dispersion of the strings found in MHM22 to a random sample of stars drawn from physically unrelated open clusters. We find that the chemical homogeneity of the strings is similar to the chemical homogeneity seen in random stellar draws across clusters.
6. The combined spatial, dynamical, and chemical evidence rules out the scenario that stars within a typical string were born at the same time within the same parental molecular gas structure. However, some subset of the stars within a string may still be co-eval, as many of these strings contain real clusters that have been linked together to form the larger string-like structure.

Ultimately, by evoking simple spatial and dynamical arguments, our work provides a straightforward, yet discerning, lens to evaluate the fidelity of newfound classes of objects, which should be considered when declaring the existence of new co-eval stellar structures in the *Gaia* era.

1 The authors would like to thank the anonymous referee for their thorough and prompt review of our manuscript. CZ
2 acknowledges that support for this work was provided by NASA through the NASA Hubble Fellowship grant #HST-
3 HF2-51498.001 awarded by the Space Telescope Science Institute (STScI), which is operated by the Association of
4 Universities for Research in Astronomy, Inc., for NASA, under contract NAS5-26555. SL acknowledges support from
5 NSF grant AST2109234 and HST-AR-16624 from STScI. The authors would like to thank Keith Hawkins, Catherine
6 Manea, Kevin Covey, Marina Kounkel, Stefan Meingast, João Alves, and Alyssa Goodman for helpful comments that
7 contributed to this work.

REFERENCES

- Andrews, J. J., Curtis, J. L., Chanamé, J., et al. 2022, *AJ*, 163, 275, doi: [10.3847/1538-3881/ac6952](https://doi.org/10.3847/1538-3881/ac6952)
- Beccari, G., Boffin, H. M. J., & Jerabkova, T. 2020, *MNRAS*, 491, 2205, doi: [10.1093/mnras/stz3195](https://doi.org/10.1093/mnras/stz3195)
- Bird, J. C., Loebman, S. R., Weinberg, D. H., et al. 2021, *MNRAS*, 503, 1815, doi: [10.1093/mnras/stab289](https://doi.org/10.1093/mnras/stab289)
- Buder, S., Sharma, S., Kos, J., et al. 2021, *MNRAS*, 506, 150, doi: [10.1093/mnras/stab1242](https://doi.org/10.1093/mnras/stab1242)
- Cantat-Gaudin, T. 2022, *Universe*, 8, 111, doi: [10.3390/universe8020111](https://doi.org/10.3390/universe8020111)
- Cantat-Gaudin, T., Mapelli, M., Balaguer-Núñez, L., et al. 2019, *A&A*, 621, A115, doi: [10.1051/0004-6361/201834003](https://doi.org/10.1051/0004-6361/201834003)
- Casagrande, L., Schönrich, R., Asplund, M., et al. 2011, *A&A*, 530, A138, doi: [10.1051/0004-6361/201016276](https://doi.org/10.1051/0004-6361/201016276)
- Castro-Ginard, A., Jordi, C., Luri, X., et al. 2020, *A&A*, 635, A45, doi: [10.1051/0004-6361/201937386](https://doi.org/10.1051/0004-6361/201937386)
- Coronado, J., Fürnkranz, V., & Rix, H.-W. 2022, *ApJ*, 928, 70, doi: [10.3847/1538-4357/ac545c](https://doi.org/10.3847/1538-4357/ac545c)
- Feng, Y., & Krumholz, M. R. 2014, *Nature*, 513, 523, doi: [10.1038/nature13662](https://doi.org/10.1038/nature13662)
- Gaia Collaboration, Prusti, T., de Bruijne, J. H. J., et al. 2016, *A&A*, 595, A1, doi: [10.1051/0004-6361/201629272](https://doi.org/10.1051/0004-6361/201629272)
- Gaia Collaboration, Brown, A. G. A., Vallenari, A., et al. 2018, *A&A*, 616, A1, doi: [10.1051/0004-6361/201833051](https://doi.org/10.1051/0004-6361/201833051)
- . 2021, *A&A*, 649, A1, doi: [10.1051/0004-6361/202039657](https://doi.org/10.1051/0004-6361/202039657)
- Gao, X., Lind, K., Amarsi, A. M., et al. 2018, *MNRAS*, 481, 2666, doi: [10.1093/mnras/sty2414](https://doi.org/10.1093/mnras/sty2414)
- Gialluca, M. T., Naidu, R. P., & Bonaca, A. 2021, *ApJL*, 911, L32, doi: [10.3847/2041-8213/abf491](https://doi.org/10.3847/2041-8213/abf491)
- Goodman, A. A., Alves, J., Beaumont, C. N., et al. 2014, *ApJ*, 797, 53, doi: [10.1088/0004-637X/797/1/53](https://doi.org/10.1088/0004-637X/797/1/53)
- Hawkins, K., Lucey, M., & Curtis, J. 2020, *MNRAS*, 496, 2422, doi: [10.1093/mnras/staa1673](https://doi.org/10.1093/mnras/staa1673)
- Jerabkova, T., Boffin, H. M. J., Beccari, G., & Anderson, R. I. 2019, *MNRAS*, 489, 4418, doi: [10.1093/mnras/stz2315](https://doi.org/10.1093/mnras/stz2315)
- Jönsson, H., Holtzman, J. A., Allende Prieto, C., et al. 2020, *AJ*, 160, 120, doi: [10.3847/1538-3881/aba592](https://doi.org/10.3847/1538-3881/aba592)
- Koukel, M., & Covey, K. 2019, *AJ*, 158, 122, doi: [10.3847/1538-3881/ab339a](https://doi.org/10.3847/1538-3881/ab339a)
- Koukel, M., Covey, K., & Stassun, K. G. 2020, *AJ*, 160, 279, doi: [10.3847/1538-3881/abc0e6](https://doi.org/10.3847/1538-3881/abc0e6)
- Kuhn, M. A., Hillenbrand, L. A., Sills, A., Feigelson, E. D., & Getman, K. V. 2019, *ApJ*, 870, 32, doi: [10.3847/1538-4357/aaef8c](https://doi.org/10.3847/1538-4357/aaef8c)
- Kuzma, P. B., Da Costa, G. S., Keller, S. C., & Maunder, E. 2015, *MNRAS*, 446, 3297, doi: [10.1093/mnras/stu2343](https://doi.org/10.1093/mnras/stu2343)
- Lada, C. J., & Lada, E. A. 2003, *ARA&A*, 41, 57, doi: [10.1146/annurev.astro.41.011802.094844](https://doi.org/10.1146/annurev.astro.41.011802.094844)
- Manea, C., Hawkins, K., & Maas, Z. G. 2022, *MNRAS*, 511, 2829, doi: [10.1093/mnras/stac236](https://doi.org/10.1093/mnras/stac236)
- Maschberger, T., Clarke, C. J., Bonnell, I. A., & Kroupa, P. 2010, *MNRAS*, 404, 1061, doi: [10.1111/j.1365-2966.2010.16346.x](https://doi.org/10.1111/j.1365-2966.2010.16346.x)
- McInnes, L., Healy, J., & Astels, S. 2017, *The Journal of Open Source Software*, 2, 205, doi: [10.21105/joss.00205](https://doi.org/10.21105/joss.00205)
- Meingast, S., & Alves, J. 2019, *A&A*, 621, L3, doi: [10.1051/0004-6361/201834622](https://doi.org/10.1051/0004-6361/201834622)
- Meingast, S., Alves, J., & Fürnkranz, V. 2019, *A&A*, 622, L13, doi: [10.1051/0004-6361/201834950](https://doi.org/10.1051/0004-6361/201834950)
- Meingast, S., Alves, J., & Rottensteiner, A. 2021, *A&A*, 645, A84, doi: [10.1051/0004-6361/202038610](https://doi.org/10.1051/0004-6361/202038610)
- Moranta, L., Gagné, J., Couture, D., & Faherty, J. K. 2022, *arXiv e-prints*, arXiv:2206.04567, <https://arxiv.org/abs/2206.04567>
- Ness, M., Rix, H. W., Hogg, D. W., et al. 2018, *ApJ*, 853, 198, doi: [10.3847/1538-4357/aa9d8e](https://doi.org/10.3847/1538-4357/aa9d8e)
- Plummer, H. C. 1911, *MNRAS*, 71, 460, doi: [10.1093/mnras/71.5.460](https://doi.org/10.1093/mnras/71.5.460)
- Portegies Zwart, S. F., McMillan, S. L. W., & Gieles, M. 2010, *ARA&A*, 48, 431, doi: [10.1146/annurev-astro-081309-130834](https://doi.org/10.1146/annurev-astro-081309-130834)
- Ragan, S. E., Henning, T., Tackenberg, J., et al. 2014, *A&A*, 568, A73, doi: [10.1051/0004-6361/201423401](https://doi.org/10.1051/0004-6361/201423401)
- Ratzenböck, S., Meingast, S., Alves, J., Möller, T., & Bomze, I. 2020, *A&A*, 639, A64, doi: [10.1051/0004-6361/202037591](https://doi.org/10.1051/0004-6361/202037591)
- Soubiran, C., Cantat-Gaudin, T., Romero-Gómez, M., et al. 2018, *A&A*, 619, A155, doi: [10.1051/0004-6361/201834020](https://doi.org/10.1051/0004-6361/201834020)
- Spina, L., Ting, Y. S., De Silva, G. M., et al. 2021, *MNRAS*, 503, 3279, doi: [10.1093/mnras/stab471](https://doi.org/10.1093/mnras/stab471)
- Tarriq, Y., Soubiran, C., Casamiquela, L., et al. 2021, *A&A*, 647, A19, doi: [10.1051/0004-6361/202039388](https://doi.org/10.1051/0004-6361/202039388)
- Taylor, M. B. 2005, in *Astronomical Society of the Pacific Conference Series*, Vol. 347, *Astronomical Data Analysis Software and Systems XIV*, ed. P. Shopbell, M. Britton, & R. Ebert, 29
- Tian, H.-J. 2020, *ApJ*, 904, 196, doi: [10.3847/1538-4357/abbf4b](https://doi.org/10.3847/1538-4357/abbf4b)
- van Leeuwen, F. 2009, *A&A*, 497, 209, doi: [10.1051/0004-6361/200811382](https://doi.org/10.1051/0004-6361/200811382)
- Wang, F., Tian, H., Qiu, D., et al. 2022, *MNRAS*, doi: [10.1093/mnras/stac843](https://doi.org/10.1093/mnras/stac843)
- Wang, K., Testi, L., Ginsburg, A., et al. 2015, *MNRAS*, 450, 4043, doi: [10.1093/mnras/stv735](https://doi.org/10.1093/mnras/stv735)

- Zucker, C., Battersby, C., & Goodman, A. 2015, ApJ, 815, 23, doi: [10.1088/0004-637X/815/1/23](https://doi.org/10.1088/0004-637X/815/1/23)
- . 2018, ApJ, 864, 153, doi: [10.3847/1538-4357/aacc66](https://doi.org/10.3847/1538-4357/aacc66)
- Zucker, C., Smith, R., & Goodman, A. 2019, ApJ, 887, 186, doi: [10.3847/1538-4357/ab517d](https://doi.org/10.3847/1538-4357/ab517d)

Table 2. Spatial and Dynamical Properties of Stellar Strings

Theia	DR2 Offset	DR2 S/N	DR3 Offset	DR3 S/N	σ_{V_r}	M_{virial}	M_{observed}	$\frac{M_{\text{virial}}}{M_{\text{observed}}}$	$t_{\text{dispersal}}$	Age	$\frac{\text{Age}}{t_{\text{dispersal}}}$
	pc		pc		km s ⁻¹	M_{\odot}	M_{\odot}		Myr	Myr	
(1)	(2)	(3)	(4)	(5)	(6)	(7)	(8)	(9)	(10)	(11)	(12)
9	35	22	28	30	29.2	5.7e+06	327	1.7e+04	1.0	4	4
13	29	31	27	52	17.8	2.1e+06	6457	3.2e+02	1.5	7	5
17	16	32	15	58	16.7	9.9e+05	194	5.1e+03	0.9	8	9
21	24	32	24	55	15.5	1.4e+06	225	6.0e+03	1.5	11	7
22	23	38	22	60	10.2	5.6e+05	1563	3.6e+02	2.2	12	5
23	31	30	31	48	53.2	2.1e+07	331	6.2e+04	0.6	12	20
28	28	26	27	34	12.7	1.0e+06	247	4.1e+03	2.1	11	5
39	33	39	31	47	10.6	8.2e+05	212	3.9e+03	2.9	15	5
40	87	27	91	38	27.4	1.6e+07	763	2.1e+04	3.3	12	3
41	28	18	25	25	28.6	4.8e+06	400	1.2e+04	0.9	12	14
43	10	97	10	214	8.9	2.0e+05	1471	1.4e+02	1.2	16	13
44	10	97	10	206	7.7	1.4e+05	161	8.9e+02	1.3	15	11
45	15	84	15	195	17.3	1.0e+06	1600	6.5e+02	0.8	15	18
53	4	72	4	152	11.1	1.1e+05	26	4.3e+03	0.4	25	70
55	44	42	43	70	17.3	3.0e+06	1017	2.9e+03	2.4	24	10
56	45	22	85	28	22.5	1.0e+07	553	1.8e+04	3.7	22	6
57	37	29	37	44	9.9	8.5e+05	1209	7.0e+02	3.7	21	5
58	43	36	43	51	15.5	2.5e+06	463	5.3e+03	2.8	25	9
72	14	39	14	64	34.9	4.0e+06	116	3.4e+04	0.4	31	78
73	33	43	31	66	16.9	2.1e+06	1873	1.1e+03	1.8	26	14
74	38	47	37	71	5.4	2.6e+05	1141	2.3e+02	6.8	31	4
75	34	50	33	71	14.5	1.6e+06	997	1.6e+03	2.3	29	12
77	18	31	16	47	20.3	1.6e+06	506	3.2e+03	0.8	26	32
79	32	47	28	62	18.3	2.2e+06	256	8.7e+03	1.5	25	16
80	21	31	23	44	11.0	6.5e+05	278	2.3e+03	2.1	26	12
81	26	26	31	36	11.2	9.1e+05	226	4.0e+03	2.7	26	9
86	22	35	21	53	9.0	4.1e+05	186	2.2e+03	2.4	25	10
87	49	36	38	53	11.5	1.2e+06	312	3.8e+03	3.3	26	7
91	44	39	38	53	15.7	2.2e+06	340	6.4e+03	2.4	26	11
92	9	114	9	205	5.3	6.1e+04	818	7.4e+01	1.7	35	20
95	25	74	24	113	16.1	1.5e+06	685	2.2e+03	1.5	33	22
96	21	46	20	70	13.5	8.7e+05	775	1.1e+03	1.5	35	23
97	25	43	24	61	21.5	2.7e+06	595	4.5e+03	1.1	33	29
98	31	52	30	75	12.1	1.0e+06	211	4.9e+03	2.4	38	15
99	44	46	45	65	23.0	5.6e+06	427	1.3e+04	1.9	32	16
108	25	44	24	63	13.9	1.1e+06	240	4.6e+03	1.7	33	19
111	41	35	41	47	15.3	2.2e+06	138	1.6e+04	2.6	32	12
113	11	201	11	396	16.2	6.7e+05	111	6.0e+03	0.7	43	64
115	27	95	27	156	14.6	1.4e+06	339	4.0e+03	1.8	44	24
116	26	56	26	92	24.3	3.6e+06	681	5.3e+03	1.1	48	45
118	23	50	23	80	15.7	1.3e+06	1133	1.2e+03	1.5	50	34
120	21	47	20	67	13.6	8.7e+05	508	1.7e+03	1.4	46	31
125	35	33	34	50	22.7	4.1e+06	340	1.2e+04	1.5	49	33
127	25	36	22	50	4.6	1.1e+05	290	3.9e+02	4.9	48	9
133	19	96	18	160	21.0	1.9e+06	1612	1.2e+03	0.9	55	64
136	8	56	7	83	7.3	9.2e+04	103	8.9e+02	1.0	50	50
138	13	38	13	57	9.3	2.6e+05	171	1.5e+03	1.4	57	41
139	29	40	31	67	19.3	2.7e+06	78	3.5e+04	1.6	51	32
143	22	54	21	77	8.5	3.6e+05	1081	3.3e+02	2.4	55	22
149	42	42	43	59	30.0	9.2e+06	442	2.1e+04	1.4	57	40
150	31	44	33	56	14.2	1.6e+06	195	8.1e+03	2.3	53	23
153	34	35	36	45	16.1	2.2e+06	186	1.2e+04	2.2	56	25
157	54	32	49	39	29.9	1.0e+07	168	6.1e+04	1.6	54	33
158	28	33	30	46	15.5	1.7e+06	162	1.0e+04	1.9	60	31
160	16	71	16	113	17.1	1.1e+06	183	6.1e+03	0.9	79	84
161	8	64	8	94	4.9	4.5e+04	93	4.8e+02	1.6	75	47
163	21	67	21	94	18.3	1.6e+06	442	3.7e+03	1.1	78	69
164	20	68	20	100	8.1	3.1e+05	194	1.6e+03	2.5	78	31
165	42	51	43	74	18.8	3.5e+06	1116	3.2e+03	2.2	71	32
166	30	45	30	62	8.9	5.6e+05	87	6.5e+03	3.4	75	22
169	31	45	34	63	10.5	8.9e+05	173	5.1e+03	3.2	78	24
174	61	42	63	52	17.0	4.3e+06	156	2.7e+04	3.7	73	20

Table 2 continued on next page

Table 2 (*continued*)

Theia	DR2 Offset	DR2 S/N	DR3 Offset	DR3 S/N	σ_{V_r}	M_{virial}	M_{observed}	$\frac{M_{\text{virial}}}{M_{\text{observed}}}$	$t_{\text{dispersal}}$	Age	$\frac{\text{Age}}{t_{\text{dispersal}}}$
	pc		pc		km s^{-1}	M_{\odot}	M_{\odot}		Myr	Myr	
(1)	(2)	(3)	(4)	(5)	(6)	(7)	(8)	(9)	(10)	(11)	(12)
182	34	28	38	42	43.4	1.7e+07	77	2.2e+05	0.9	67	78
189	50	30	50	47	17.7	3.7e+06	205	1.8e+04	2.8	71	25
190	92	22	107	35	45.8	5.2e+07	361	1.4e+05	2.3	72	31
195	87	21	92	34	36.1	2.8e+07	584	4.8e+04	2.5	70	28
205	26	30	32	42	15.7	1.9e+06	105	1.8e+04	2.0	70	34
208	11	217	11	478	19.8	1.1e+06	67	1.6e+04	0.6	94	163
213	31	74	32	103	8.9	6.0e+05	90	6.7e+03	3.6	97	27
214	19	57	19	82	18.6	1.6e+06	170	9.1e+03	1.0	96	95
215	29	84	28	121	34.4	7.7e+06	278	2.8e+04	0.8	91	114
216	13	61	13	84	5.8	1.1e+05	269	3.9e+02	2.3	97	42
219	25	57	24	88	17.8	1.8e+06	160	1.1e+04	1.3	94	70
228	24	45	29	58	8.2	4.6e+05	104	4.4e+03	3.6	96	27
233	58	53	60	73	12.0	2.0e+06	376	5.4e+03	4.9	80	16
236	41	43	43	64	19.9	4.0e+06	133	3.0e+04	2.1	84	39
237	38	49	40	71	13.2	1.6e+06	81	2.0e+04	3.0	79	26
244	30	63	27	93	19.9	2.5e+06	76	3.2e+04	1.3	82	62
245	18	71	18	101	11.0	5.3e+05	93	5.7e+03	1.7	90	53
246	30	47	32	66	11.2	9.4e+05	266	3.5e+03	2.8	80	28
248	60	46	58	63	12.4	2.1e+06	330	6.4e+03	4.6	93	20
250	16	45	15	68	9.9	3.5e+05	107	3.3e+03	1.5	81	53
252	66	35	81	50	20.0	7.6e+06	208	3.6e+04	4.0	87	21
253	66	44	69	61	12.1	2.4e+06	100	2.3e+04	5.6	87	15
254	46	35	44	49	25.6	6.8e+06	707	9.6e+03	1.7	99	58
259	22	37	25	48	10.0	5.8e+05	81	7.1e+03	2.5	88	35
261	37	27	38	41	21.1	4.0e+06	159	2.5e+04	1.8	93	52
262	35	39	38	52	10.5	9.9e+05	104	9.4e+03	3.5	85	24
263	38	41	33	59	25.3	5.0e+06	197	2.5e+04	1.3	92	70
275	72	25	60	42	21.5	6.5e+06	90	7.2e+04	2.8	82	29
282	55	25	49	40	17.9	3.6e+06	203	1.8e+04	2.7	86	32
285	55	29	60	38	19.1	5.1e+06	238	2.2e+04	3.1	82	26
291	57	22	67	35	36.7	2.1e+07	328	6.4e+04	1.8	86	48
294	34	24	33	39	12.3	1.2e+06	731	1.6e+03	2.7	79	29
301	24	125	24	191	13.0	9.7e+05	801	1.2e+03	1.9	106	57
303	19	74	18	129	25.1	2.7e+06	204	1.3e+04	0.7	107	149
305	9	78	7	110	15.2	3.9e+05	25	1.6e+04	0.5	122	259
306	19	45	18	61	9.1	3.5e+05	43	7.9e+03	1.9	106	55
308	14	66	14	97	16.3	9.0e+05	78	1.1e+04	0.9	110	128
309	24	58	24	78	12.8	9.3e+05	355	2.6e+03	1.8	109	59
310	26	57	26	76	15.8	1.5e+06	101	1.5e+04	1.7	105	64
311	38	50	36	72	14.7	1.8e+06	264	6.9e+03	2.4	106	43
312	18	42	18	61	13.7	8.0e+05	62	1.3e+04	1.3	100	77
316	40	30	46	42	39.6	1.7e+07	211	8.0e+04	1.1	107	94
325	58	30	57	48	11.5	1.8e+06	659	2.7e+03	4.9	116	23
326	37	30	40	45	18.1	3.0e+06	68	4.5e+04	2.2	119	55
327	42	44	39	60	19.1	3.3e+06	206	1.6e+04	2.0	101	50
329	43	31	44	50	29.5	9.0e+06	125	7.2e+04	1.5	101	68
331	23	44	20	64	12.8	8.0e+05	371	2.2e+03	1.6	109	68
334	34	28	26	44	16.2	1.6e+06	217	7.4e+03	1.6	106	66
339	41	33	40	47	11.6	1.3e+06	134	9.3e+03	3.4	114	33
342	29	30	29	45	12.9	1.1e+06	152	7.4e+03	2.2	101	46
344	39	28	42	42	31.4	9.8e+06	64	1.5e+05	1.3	111	83
348	43	27	43	44	17.6	3.2e+06	431	7.3e+03	2.4	116	47
349	51	36	49	49	29.1	9.7e+06	434	2.2e+04	1.7	102	62
353	73	28	81	40	21.5	8.8e+06	365	2.4e+04	3.7	105	28
354	86	23	91	36	12.9	3.5e+06	436	8.0e+03	6.9	106	15
357	60	22	57	30	13.4	2.4e+06	131	1.8e+04	4.2	114	27
358	68	36	63	51	13.7	2.8e+06	149	1.8e+04	4.6	108	23
363	48	24	39	33	11.2	1.1e+06	114	1.0e+04	3.4	105	31
368	9	88	8	155	13.8	3.7e+05	77	4.8e+03	0.6	126	213
372	17	70	17	123	13.3	7.3e+05	84	8.7e+03	1.3	150	115
375	15	64	13	112	18.2	1.1e+06	32	3.3e+04	0.8	130	173
379	30	47	28	75	26.7	4.8e+06	431	1.1e+04	1.1	137	129
380	24	41	25	66	11.8	8.4e+05	169	4.9e+03	2.1	131	62
384	56	44	58	56	36.3	1.8e+07	286	6.2e+04	1.6	143	91

Table 2 *continued on next page*

Table 2 (*continued*)

Theia	DR2 Offset	DR2 S/N	DR3 Offset	DR3 S/N	σ_{V_r}	M_{virial}	M_{observed}	$\frac{M_{\text{virial}}}{M_{\text{observed}}}$	$t_{\text{dispersal}}$	Age	$\frac{\text{Age}}{t_{\text{dispersal}}}$
	pc		pc		km s^{-1}	M_{\odot}	M_{\odot}		Myr	Myr	
(1)	(2)	(3)	(4)	(5)	(6)	(7)	(8)	(9)	(10)	(11)	(12)
388	30	43	30	59	10.6	8.1e+05	290	2.8e+03	2.8	137	48
389	35	31	31	47	17.9	2.4e+06	111	2.1e+04	1.7	142	82
390	34	32	33	51	19.9	3.1e+06	301	1.0e+04	1.6	132	82
391	46	39	44	58	12.7	1.7e+06	389	4.3e+03	3.5	148	42
400	81	26	77	40	19.9	7.2e+06	84	8.5e+04	3.8	127	33
403	57	25	60	39	41.6	2.5e+07	90	2.7e+05	1.4	145	101
405	72	30	69	44	19.8	6.3e+06	569	1.1e+04	3.4	141	41
407	25	25	23	44	29.8	4.8e+06	392	1.2e+04	0.8	138	180
421	67	28	66	37	16.2	4.1e+06	223	1.8e+04	4.0	139	35
424	6	209	6	394	7.2	7.9e+04	91	8.6e+02	0.9	189	210
428	13	121	12	174	18.4	1.0e+06	61	1.6e+04	0.7	180	268
430	11	88	11	139	8.2	1.8e+05	130	1.3e+03	1.4	190	140
431	20	74	20	119	34.4	5.7e+06	181	3.1e+04	0.6	191	328
432	13	80	14	121	10.8	4.0e+05	46	8.6e+03	1.3	173	131
433	33	62	32	90	18.3	2.5e+06	255	1.0e+04	1.8	187	107
435	15	66	15	106	27.7	2.8e+06	416	6.8e+03	0.6	176	315
436	22	76	23	107	13.2	9.5e+05	101	9.4e+03	1.7	172	99
438	22	60	22	98	24.4	3.1e+06	85	3.6e+04	0.9	174	196
439	24	60	24	82	13.6	1.0e+06	376	2.8e+03	1.8	182	104
441	31	45	34	71	26.8	5.8e+06	170	3.4e+04	1.3	188	148
443	26	44	26	58	25.6	4.0e+06	342	1.2e+04	1.0	189	190
445	28	48	25	64	12.5	9.5e+05	202	4.7e+03	2.0	188	92
446	25	47	28	63	9.2	5.7e+05	161	3.6e+03	3.1	184	60
447	35	47	31	69	13.3	1.3e+06	354	3.6e+03	2.3	174	75
448	41	41	42	60	12.7	1.6e+06	151	1.0e+04	3.2	160	49
450	37	38	38	52	25.3	5.8e+06	358	1.6e+04	1.5	191	127
452	44	44	45	62	12.8	1.7e+06	675	2.5e+03	3.5	170	49
453	31	54	32	75	21.7	3.5e+06	331	1.1e+04	1.4	172	119
455	53	45	51	58	13.7	2.2e+06	131	1.7e+04	3.7	190	51
456	25	36	21	58	7.9	3.1e+05	285	1.1e+03	2.7	165	61
459	59	27	65	42	27.0	1.1e+07	523	2.1e+04	2.4	164	69
463	54	29	53	44	12.0	1.8e+06	170	1.0e+04	4.4	178	40
464	22	40	23	57	7.0	2.7e+05	103	2.6e+03	3.3	178	54
468	54	29	55	45	28.4	1.0e+07	98	1.0e+05	1.9	175	92
490	82	36	78	49	25.7	1.2e+07	120	1.0e+05	3.0	172	57
492	52	30	43	43	15.6	2.5e+06	86	2.9e+04	2.7	189	69
499	49	31	49	45	12.9	1.9e+06	173	1.1e+04	3.8	198	52
503	41	29	31	38	20.7	3.2e+06	184	1.7e+04	1.5	170	112
506	14	209	14	372	20.4	1.5e+06	278	5.2e+03	0.7	214	298
507	14	156	14	259	14.8	7.3e+05	157	4.7e+03	1.0	200	210
508	17	134	16	225	22.2	1.9e+06	122	1.6e+04	0.7	232	313
509	25	111	25	190	16.7	1.7e+06	316	5.3e+03	1.5	245	162
510	7	128	6	175	31.4	1.5e+06	37	4.1e+04	0.2	233	1143
516	32	59	35	78	16.5	2.2e+06	129	1.7e+04	2.1	239	114
520	29	67	30	86	12.8	1.2e+06	242	4.8e+03	2.3	246	106
521	32	54	35	78	8.3	5.6e+05	75	7.4e+03	4.2	243	58
527	64	46	67	64	25.9	1.1e+07	231	4.5e+04	2.5	218	86
532	28	45	26	63	14.0	1.2e+06	45	2.6e+04	1.9	243	131
534	50	45	49	61	22.1	5.6e+06	305	1.8e+04	2.2	217	99
536	44	35	47	55	14.5	2.3e+06	289	7.9e+03	3.2	227	71
550	31	32	29	42	24.0	3.9e+06	68	5.7e+04	1.2	235	196
564	76	34	78	43	19.2	6.7e+06	95	7.0e+04	4.0	209	52
595	24	123	24	231	22.7	2.9e+06	414	7.1e+03	1.1	290	273
598	20	65	21	102	11.5	6.5e+05	389	1.7e+03	1.8	290	162
599	25	80	26	115	17.5	1.9e+06	387	4.8e+03	1.5	264	178
601	15	63	16	94	21.5	1.7e+06	35	4.9e+04	0.7	273	373
603	25	56	25	81	12.3	8.9e+05	112	7.9e+03	2.0	309	154
605	26	81	26	114	4.3	1.1e+05	245	4.5e+02	6.0	288	48
607	23	50	23	71	16.0	1.4e+06	164	8.4e+03	1.4	297	210
613	11	60	10	76	8.9	2.0e+05	1831	1.1e+02	1.2	251	210
616	52	47	54	64	27.4	9.4e+06	438	2.2e+04	1.9	259	134
621	25	59	27	80	12.0	9.4e+05	63	1.5e+04	2.3	291	128
624	50	38	52	62	22.7	6.3e+06	550	1.2e+04	2.3	302	133
663	39	30	42	43	18.1	3.2e+06	131	2.4e+04	2.3	267	117

Table 2 *continued on next page*

Table 2 (*continued*)

Theia	DR2 Offset	DR2 S/N	DR3 Offset	DR3 S/N	σ_{V_r}	M_{virial}	M_{observed}	$\frac{M_{\text{virial}}}{M_{\text{observed}}}$	$t_{\text{dispersal}}$	Age	$\frac{\text{Age}}{t_{\text{dispersal}}}$
	pc		pc		km s^{-1}	M_{\odot}	M_{\odot}		Myr	Myr	
(1)	(2)	(3)	(4)	(5)	(6)	(7)	(8)	(9)	(10)	(11)	(12)
676	12	147	13	281	18.8	1.1e+06	113	9.4e+03	0.7	370	546
677	11	159	11	265	18.7	9.3e+05	65	1.4e+04	0.6	371	618
678	32	113	32	185	15.5	1.8e+06	495	3.6e+03	2.0	327	162
679	17	80	16	144	19.4	1.5e+06	84	1.7e+04	0.8	339	402
680	15	64	17	91	7.3	2.2e+05	34	6.3e+03	2.3	364	155
683	19	61	19	87	18.7	1.6e+06	129	1.2e+04	1.0	358	355
684	14	66	15	113	11.2	4.5e+05	141	3.2e+03	1.3	364	272
685	36	73	36	99	17.7	2.6e+06	404	6.6e+03	2.0	355	177
695	19	47	18	76	34.7	5.3e+06	86	6.1e+04	0.5	354	666
702	36	64	36	92	13.9	1.6e+06	68	2.4e+04	2.6	347	135
704	19	67	18	94	8.0	2.7e+05	80	3.4e+03	2.2	326	147
706	47	52	50	65	17.8	3.7e+06	236	1.6e+04	2.7	336	122
707	43	53	39	67	24.0	5.3e+06	89	5.9e+04	1.6	322	199
709	28	36	28	52	15.6	1.6e+06	93	1.7e+04	1.8	371	209
719	19	36	20	50	11.9	6.8e+05	61	1.1e+04	1.7	361	213
724	28	40	29	53	10.2	7.1e+05	170	4.1e+03	2.8	354	125
727	41	36	42	58	39.0	1.5e+07	186	8.1e+04	1.1	392	366
730	45	39	43	54	20.2	4.1e+06	281	1.5e+04	2.1	335	160
734	45	31	52	42	25.4	7.9e+06	62	1.3e+05	2.0	371	185
741	37	28	28	42	15.9	1.7e+06	112	1.5e+04	1.7	344	198
778	39	36	28	48	10.2	6.9e+05	563	1.2e+03	2.7	388	141
786	18	108	18	169	25.4	2.8e+06	152	1.8e+04	0.7	461	647
787	13	90	13	127	23.8	1.7e+06	266	6.5e+03	0.5	440	817
791	22	83	23	127	19.2	2.0e+06	101	1.9e+04	1.2	479	408
792	11	65	11	113	25.4	1.8e+06	129	1.4e+04	0.5	414	898
793	33	80	33	121	11.1	9.6e+05	112	8.6e+03	2.9	424	144
794	14	94	13	133	21.7	1.5e+06	46	3.2e+04	0.6	423	682
796	22	83	22	112	14.0	1.0e+06	115	8.7e+03	1.5	454	295
798	11	111	12	149	28.7	2.3e+06	31	7.4e+04	0.4	415	993
805	15	67	15	100	17.6	1.1e+06	37	3.1e+04	0.9	410	466
809	29	50	30	81	16.3	1.9e+06	115	1.7e+04	1.8	425	230
810	47	46	45	65	14.1	2.1e+06	178	1.2e+04	3.2	441	138
818	26	39	19	55	11.4	5.9e+05	53	1.1e+04	1.7	438	264
819	40	48	41	60	15.1	2.2e+06	133	1.6e+04	2.7	426	159
822	53	42	53	58	14.0	2.5e+06	426	5.8e+03	3.7	404	107
823	13	47	13	72	12.1	4.5e+05	254	1.8e+03	1.1	417	387
825	48	41	47	64	30.8	1.1e+07	117	9.0e+04	1.5	426	281
831	55	32	58	44	30.0	1.2e+07	194	6.4e+04	1.9	418	217
847	29	32	30	46	6.1	2.7e+05	289	9.4e+02	4.9	449	91
848	22	27	16	43	8.9	3.1e+05	958	3.2e+02	1.8	428	237
857	50	37	53	55	8.3	8.6e+05	408	2.1e+03	6.3	474	75
874	45	25	44	41	35.9	1.3e+07	132	1.0e+05	1.2	441	363
904	55	30	51	40	12.2	1.8e+06	339	5.3e+03	4.2	494	118
905	20	120	20	191	21.8	2.3e+06	121	1.9e+04	0.9	538	575
906	25	142	25	225	19.6	2.3e+06	340	6.8e+03	1.3	503	391
908	44	89	45	129	16.3	2.8e+06	329	8.4e+03	2.7	611	226
912	27	50	27	74	14.1	1.3e+06	109	1.2e+04	1.9	505	263
914	44	39	39	54	25.2	5.8e+06	52	1.1e+05	1.5	618	405
920	16	37	17	58	19.5	1.5e+06	66	2.3e+04	0.9	501	587
921	22	55	22	71	15.2	1.2e+06	28	4.4e+04	1.5	537	363
930	46	38	46	47	19.4	4.1e+06	176	2.3e+04	2.3	616	263
936	53	54	56	70	11.6	1.8e+06	111	1.6e+04	4.7	543	114
944	55	44	56	61	13.5	2.4e+06	517	4.6e+03	4.1	557	135
953	73	42	82	57	35.6	2.4e+07	78	3.1e+05	2.3	618	272
959	94	26	103	39	17.1	7.1e+06	109	6.5e+04	5.9	625	106
965	47	32	50	44	13.6	2.2e+06	56	3.9e+04	3.6	565	155
998	53	29	39	45	3.0	8.4e+04	52	1.6e+03	12.6	511	40
1005	6	221	6	358	13.9	2.9e+05	45	6.2e+03	0.4	631	1421
1007	20	87	20	151	28.6	3.9e+06	186	2.1e+04	0.7	775	1092
1008	25	105	24	146	15.3	1.4e+06	186	7.3e+03	1.6	732	461
1009	18	61	18	96	15.5	1.0e+06	29	3.5e+04	1.2	698	600
1012	24	42	22	66	5.5	1.6e+05	112	1.4e+03	4.0	660	163
1014	45	43	42	60	13.3	1.8e+06	56	3.1e+04	3.2	756	239
1015	39	40	41	54	24.7	5.9e+06	100	5.9e+04	1.6	784	481

Table 2 *continued on next page*

Table 2 (continued)

Theia	DR2 Offset	DR2 S/N	DR3 Offset	DR3 S/N	σ_{V_r}	M_{virial}	M_{observed}	$\frac{M_{\text{virial}}}{M_{\text{observed}}}$	$t_{\text{dispersal}}$	Age	$\frac{\text{Age}}{t_{\text{dispersal}}}$
	pc		pc		km s^{-1}	M_{\odot}	M_{\odot}		Myr	Myr	
(1)	(2)	(3)	(4)	(5)	(6)	(7)	(8)	(9)	(10)	(11)	(12)
1024	27	45	28	58	13.2	1.2e+06	100	1.2e+04	2.1	641	300
1028	20	52	21	69	14.0	9.6e+05	229	4.2e+03	1.5	641	434
1059	63	28	65	36	14.9	3.4e+06	42	8.0e+04	4.3	783	182
1089	16	134	16	207	29.5	3.4e+06	113	3.0e+04	0.6	862	1556
1090	13	158	12	253	15.2	6.7e+05	23	2.8e+04	0.8	960	1208
1098	41	55	40	76	12.8	1.5e+06	112	1.4e+04	3.1	947	302
1102	43	37	42	47	15.2	2.3e+06	45	5.1e+04	2.7	794	288
1104	32	47	33	90	9.0	6.4e+05	25	2.5e+04	3.7	805	220
1107	27	56	29	70	16.2	1.8e+06	63	2.8e+04	1.8	963	548
1110	26	47	20	73	15.7	1.2e+06	34	3.5e+04	1.3	903	698
1129	26	37	25	51	9.2	5.1e+05	54	9.4e+03	2.8	815	296
1181	18	78	17	127	18.0	1.3e+06	25	5.3e+04	1.0	1237	1279
1183	12	93	12	147	10.1	2.9e+05	34	8.4e+03	1.2	1170	982
1186	30	47	30	66	15.5	1.7e+06	30	5.6e+04	1.9	1135	591
1194	21	60	24	77	13.8	1.1e+06	31	3.4e+04	1.7	1094	626
1198	37	50	35	66	11.9	1.2e+06	64	1.8e+04	3.0	1059	358
1200	32	44	38	69	34.5	1.1e+07	42	2.5e+05	1.1	1159	1067
1204	31	38	34	52	33.3	8.8e+06	30	2.9e+05	1.0	1023	1022
1208	43	42	44	58	18.7	3.6e+06	64	5.6e+04	2.3	1082	463
1214	33	40	32	67	17.7	2.4e+06	369	6.4e+03	1.8	1247	685
1216	44	27	58	33	38.8	2.0e+07	27	7.4e+05	1.5	1000	678
1217	48	38	49	49	38.9	1.7e+07	24	7.1e+05	1.2	1040	844
1232	72	37	73	47	12.3	2.6e+06	229	1.1e+04	5.8	1247	214
1243	82	28	90	40	19.4	7.9e+06	37	2.1e+05	4.5	1079	237
1269	50	20	52	27	18.7	4.3e+06	25	1.7e+05	2.8	1139	413
1275	29	125	28	194	16.2	1.8e+06	126	1.4e+04	1.7	1502	859
1278	21	66	23	87	15.2	1.3e+06	35	3.6e+04	1.5	1311	848
1283	41	64	47	72	8.2	7.3e+05	59	1.2e+04	5.7	1443	254
1285	48	36	49	50	15.7	2.8e+06	165	1.7e+04	3.1	1518	496
1286	36	51	37	63	17.7	2.7e+06	81	3.4e+04	2.1	1439	692
1295	63	32	59	44	28.2	1.1e+07	181	6.1e+04	2.1	1544	743
1299	52	30	49	47	14.6	2.5e+06	77	3.2e+04	3.3	1301	391
1300	55	36	58	51	15.9	3.4e+06	137	2.5e+04	3.6	1284	360
1312	80	28	76	42	41.0	3.0e+07	26	1.1e+06	1.8	1309	718
1313	81	42	85	53	12.8	3.3e+06	43	7.5e+04	6.5	1296	198
1315	56	41	54	48	19.6	4.9e+06	79	6.2e+04	2.7	1269	468
1327	65	35	64	42	25.3	9.6e+06	39	2.4e+05	2.5	1488	593
1352	17	56	18	82	32.9	4.7e+06	26	1.8e+05	0.5	1682	3074
1355	18	54	21	87	21.4	2.2e+06	32	6.8e+04	1.0	1584	1653
1360	38	47	38	55	17.2	2.7e+06	35	7.6e+04	2.2	1682	764
1362	31	50	33	92	23.5	4.3e+06	76	5.6e+04	1.4	1769	1286
1377	38	47	38	56	23.6	4.9e+06	57	8.5e+04	1.6	1788	1130
1378	49	37	49	57	16.9	3.3e+06	118	2.8e+04	2.9	1730	601
1379	22	15	53	18	20.0	4.9e+06	53	9.3e+04	2.6	1603	614
1385	53	34	53	40	13.3	2.2e+06	100	2.2e+04	3.9	1690	433
1394	25	36	25	48	10.8	6.9e+05	114	6.0e+03	2.3	1834	790
1397	51	45	51	59	17.5	3.7e+06	76	4.8e+04	2.9	1651	571
1404	71	37	72	49	22.1	8.3e+06	361	2.3e+04	3.2	1631	506
1415	59	29	61	42	18.7	5.0e+06	161	3.1e+04	3.2	1716	534
1416	63	30	69	36	23.3	8.8e+06	124	7.1e+04	2.9	1876	638
1439	83	31	80	41	13.9	3.6e+06	82	4.3e+04	5.6	1586	280
1455	84	41	78	59	17.1	5.4e+06	63	8.5e+04	4.5	1832	406
1459	49	24	49	31	17.8	3.7e+06	35	1.0e+05	2.7	1839	671
1476	36	88	37	105	29.4	7.4e+06	31	2.4e+05	1.2	2404	1942
1479	27	32	31	40	18.6	2.5e+06	26	9.5e+04	1.7	2089	1254
1521	53	36	46	45	12.1	1.6e+06	47	3.3e+04	3.8	2124	559
1528	14	73	14	87	13.3	5.9e+05	19	3.0e+04	1.0	2611	2489
1532	71	42	72	58	35.4	2.1e+07	218	9.6e+04	2.0	2597	1301
1535	47	44	46	53	30.9	1.0e+07	38	2.7e+05	1.5	2580	1750
1540	50	57	48	75	19.3	4.2e+06	32	1.3e+05	2.5	2828	1153
1542	53	43	46	55	17.6	3.3e+06	32	1.0e+05	2.6	2530	976
1547	59	28	63	34	32.2	1.5e+07	33	4.6e+05	1.9	2967	1529
1571	13	63	14	97	31.4	3.3e+06	24	1.4e+05	0.5	3570	7885
1576	45	37	48	46	19.6	4.3e+06	51	8.3e+04	2.4	3213	1332

Table 2 continued on next page

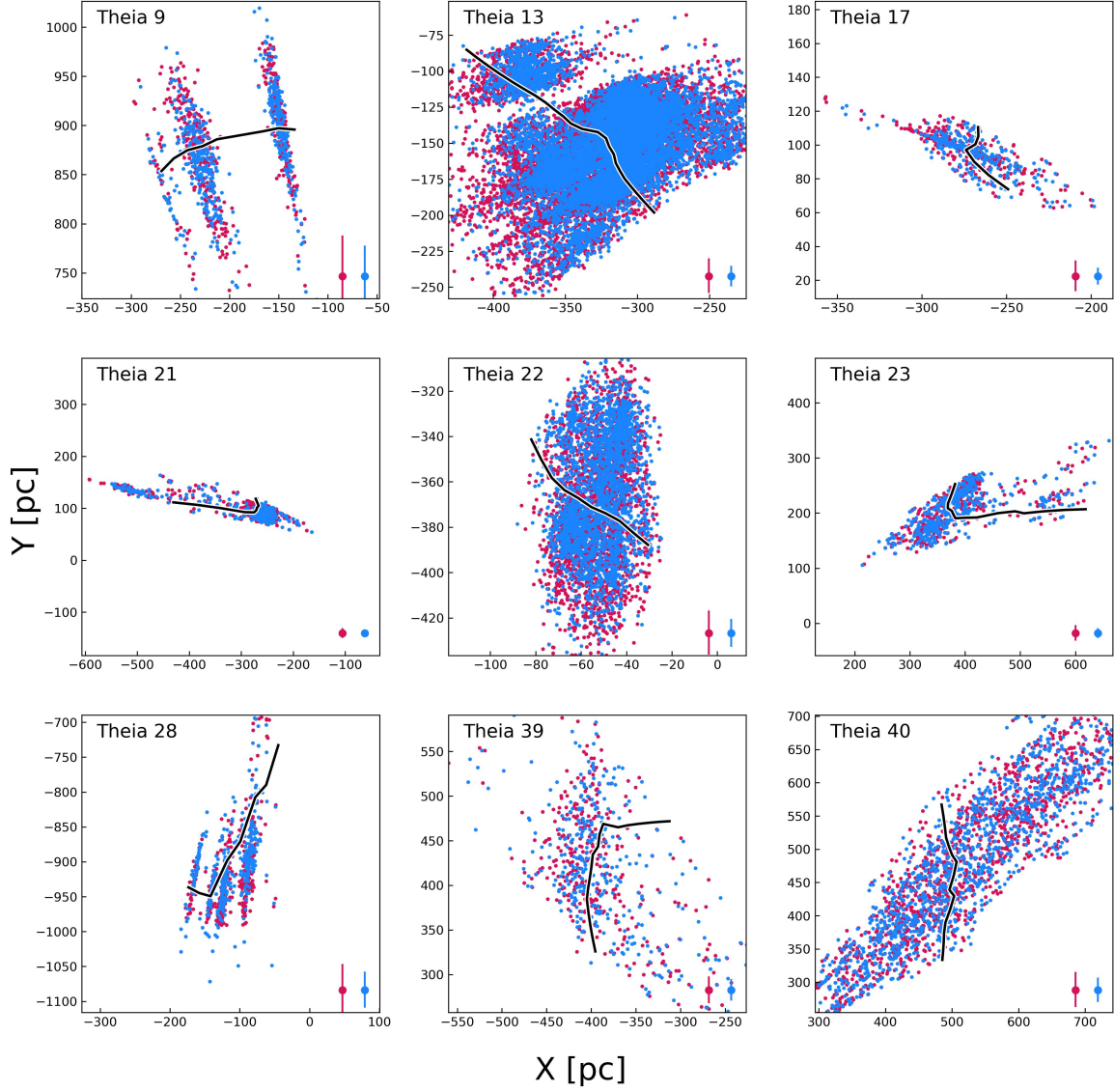
Table 2 (*continued*)

Theia	DR2 Offset	DR2 S/N	DR3 Offset	DR3 S/N	σ_{V_r}	M_{virial}	M_{observed}	$\frac{M_{\text{virial}}}{M_{\text{observed}}}$	$t_{\text{dispersal}}$	Age	$\frac{\text{Age}}{t_{\text{dispersal}}}$
	pc		pc		km s^{-1}	M_{\odot}	M_{\odot}		Myr	Myr	
(1)	(2)	(3)	(4)	(5)	(6)	(7)	(8)	(9)	(10)	(11)	(12)
1579	60	42	64	54	14.4	3.1e+06	44	7.0e+04	4.3	3559	821
1580	52	38	49	44	27.4	8.6e+06	87	9.9e+04	1.8	3228	1823
1583	48	41	47	47	15.2	2.5e+06	25	9.9e+04	3.0	3534	1168
1585	57	32	59	47	20.2	5.6e+06	48	1.2e+05	2.9	3946	1366
1595	52	31	54	41	21.5	5.8e+06	31	1.9e+05	2.5	3176	1289
1611	63	60	55	77	21.0	5.7e+06	38	1.5e+05	2.6	4664	1790
1619	55	44	49	54	21.1	5.1e+06	34	1.5e+05	2.3	4108	1798
1630	66	58	70	89	33.5	1.8e+07	30	6.1e+05	2.1	5291	2567
1634	58	46	57	66	11.6	1.8e+06	28	6.5e+04	4.9	7138	1460
1640	86	31	91	40	20.2	8.6e+06	25	3.4e+05	4.4	8969	2032

NOTE—Summary of the spatial and dynamical properties of the strings. (1) Name of the string, as given in Kounkel & Covey (2019). (2) Median *Gaia* DR2 distance offset (in parsecs) between stars in the string and the closest point on the string spine. (3) Median signal to noise of the parallax measurements of the string members in *Gaia* DR2. (4) Median *Gaia* DR3 distance offset (in parsecs) between stars in the string and the closest point on the string spine. (5) Median signal to noise of the parallax measurements of the string members in *Gaia* DR3. (6) Error-weighted radial velocity dispersion of the subset of stars in the string with *Gaia* DR3 radial velocity data, after removing flagged binaries. (7) Predicted virial mass of the string defined using the radial velocity dispersion. (8) The estimated observed mass of the string, computed by counting the number of stellar members and assuming a mean stellar mass of $0.61 M_{\odot}$ per member. (9) The ratio of the string's virial mass to its observed mass. (10) The predicted dispersal time of the string given its unbound state, defined as the crossing time (ratio of Column 4 over Column 6). (11) Reported age of the string in Kounkel & Covey (2019) (see their Table 2). (12) Ratio of the reported age of the string over the dispersal time.

APPENDIX

A. GALLERY OF STELLAR STRINGS

Fig. Set A1. Stellar Strings Gallery**Figure A1.** Top-down view of stellar strings, with each panel showing the *Gaia* DR2 (red) and *Gaia* DR3 (blue) stellar distribution of stars in the string, alongside the “spine” shown in black. The lower right hand corner of each panel shows the typical distance errors for stars in the string. An online version of this figure set is available [here](#).